IEEE Robotics and Automation Letters (RA-L) paper, presented at ICRA 2026, Vienna, Austria. Cite as RA-L paper.

Improving Gecko Adhesive Performance in Robotic Systems Through Trajectory Optimization

Dror Kobo, Goren Gordon, and Bat-El Pinchasik

***Abstract*—Gecko-inspired adhesives have attracted considerable attention due to their unique combination of strong, yet reversible adhesion to diverse surfaces. However, their integration into robotic systems remains limited due to sensitivity to contact alignment, typically requiring near-perpendicular engagement. Yet, many robotic tasks involve varying approach and detachment angles, highlighting the need for adhesion that operates reliably across different orientations and loading conditions. This study addresses two key questions: Can the adhesion strength of gecko-inspired adhesives, integrated into robotic systems, be optimized using trajectory optimization? And is this optimization surface-dependent? A gecko-inspired adhesive was integrated on a robotic arm's end-effector, which attached to and detached from surfaces along various trajectories. The arm's energy expenditure for each attachment-detachment cycle, along with the corresponding adhesion strength, were measured. Online particle swarm optimization algorithm was applied to identify conditions that improve adhesion strength and facilitate detachment. Results show that trajectory optimization significantly improves both adhesion strength and detachment efficiency up to 17-fold, with surface-specific effectiveness. These findings underscore the importance of considering both the forces generated by gecko-inspired adhesives and the energy required by the robot to attach and detach from surfaces at various angles and positions. Using optimization, this study helps overcome current limitations in the use of gecko-inspired adhesives for robotic applications, including grippers and climbers.**

***Index Terms*—Physical dry adhesive, gecko tape, bio-inspired robotics, particle swarm optimization, trajectory optimization, climbing robots, robotic grippers.**

I. Introduction

GECKO-INSPIRED adhesion, often referred to as physical or dry adhesion, has been studied for decades [1], [2], [3]. It provides a normal adhesion strength of up to a few hundred kPa [6] and a shear adhesion strength of up to a few dozen kPa [7], [8]. Since this adhesion mechanism is based on the contact area the adhesive forms with a counter surface [9], it depends on the ability to adapt to surfaces of different architectures and roughness [10], and contaminants on both surfaces [11].

The fundamentals of the gecko-inspired adhesion mechanism have been well studied [12], [13], [14], [15], [16], yet efforts to implement them in robotic systems such as grippers [17], [18], [19], and space applications [21], [22] continue to be on the rise [23], [24]. Furthermore, the implementation of gecko-inspired adhesion for walking and climbing robots remains a challenge for three main reasons [7]. First, real surfaces often have contaminants such as dust, mold, sand, and grease [11], [25]. Second, the microscale roughness and surface architecture can vary and change during robot operation [26]. Third, macroscale features such as curved surfaces, edges, and corners encountered by the robot pose significant challenges to maintain sufficient contact. Therefore, on-site decision making and trajectory optimization are crucial for improving the performance of gecko-inspired adhesives and making them suitable for robotic applications.

Applications that will greatly benefit from the use of the strong, yet reversible dry adhesion include robotic grippers [27], [28] for pick-and-place tasks, and automized attachment of objects to surfaces using robots, and robotic climbers [29], [30], [31], [32], [33], [34], [35], [36], often designed for window cleaning [37]. Other applications include surface inspection where reachability is limited or challenging [38], [39], and various space systems [21]. In terms of attaching objects, these are essential in industrial assembly, maintenance, and inspection, such as mounting components on the undersides of vehicles, aircraft, or ceilings—and in bioinspired climbing and space robotics, where robots operate on arbitrarily inclined surfaces.

Drawing from fracture mechanics, gecko-inspired adhesion is modeled as the resistance to interfacial crack propagation, with detachment occurring when the energy release rate G exceeds the critical threshold G_c. The latter depends on material properties such as Young's modulus and fibril geometry, as well as on counter-surface properties such as roughness. Following Kendall's peeling energy, and incorporating an effective compliance factor to account for the gecko-tape deformability, the available energy per area for crack propagation, G $(\mathrm{J/m^2})$ is given by the following equation [46], [47], [48], [49]:

$$G(\delta, \theta_k) \propto W k_{\text{eff}}\, \delta\, (1 - \cos\theta_k) \tag{1}$$

where W is the work of adhesion $(\mathrm{J/m^2})$, k_{eff} is a dimensionless design parameter that depends on fibril stiffness and geometry, δ is a dimensionless loading parameter (the applied preload

Received 30 June 2025; accepted 16 November 2025. Date of publication 11 December 2025; date of current version 22 December 2025. This article was recommended for publication by Associate Editor Q. Fan and Editor X. Liu upon evaluation of the reviewers' comments. *(Corresponding author: Bat-El Pinchasik.)*

Dror Kobo and Bat-El Pinchasik are with the School of Mechanical Engineering, Tel Aviv University, Tel Aviv 6116301, Israel (e-mail: pinchasik@tauex.tau.ac.il).

Goren Gordon is with the School of Industrial and Intelligent Systems Engineering, Tel Aviv University, Tel Aviv 6116301, Israel, and also with the Luddy School of Informatics, Computing, and Engineering, Indiana University, Bloomington, IN 47405 USA.

This article has supplementary downloadable material available at https://doi.org/10.1109/LRA.2025.3643330, provided by the authors.

Digital Object Identifier 10.1109/LRA.2025.3643330

IEEE Robotics and Automation Letters (RA-L) paper, presented at ICRA 2026, Vienna, Austria. Cite as RA-L paper.

deformation), and θ_k is a dynamically adjusted control parameter. Specifically, $\theta_k = 90°$ corresponds to normal pull-off, and $\theta_k = 0°$ corresponds to side peeling. In this study, we evaluate the energy expenditure of the robotic manipulator arm, which includes G, but is also governed by internal friction and losses of the robotic system, gravity, the spatial position of the manipulator arm and end-effector, and thus cannot be isolated.

Still, the main open questions remain. First, how performance can be improved to attach and detach from surfaces in an optimal way in order to maximize the adhesion strength and facilitate detachment. Second, how can a robot better perform on "real-world" surfaces, which are very often inhomogeneous. While a variety of engineered gecko-inspired adhesives exist in the market, trajectory optimization presents the most promising avenue for further improving the performance of these adhesives in robotic systems [44], [45].

In this study, we use a robotic manipulator arm to optimize the performance of a gecko-inspired adhesive integrated into the arm, interacting with a variety of surfaces. Specifically, trajectory families are evaluated according to the interface states they induce. Namely, the instantaneous spatial posture and the resultant normal and shear stresses, which govern the onset and progression of interfacial crack, promoting detachment of the gecko-inspired adhesive. We maximize the adhesion strength through an optimized approach trajectory, and minimize it through an optimized retraction trajectory, thereby enhancing adhesion strength and facilitating easier detachment, respectively.

II. Materials and Methods

A. Experimental Setup

The experimental setup consists of a six degrees of freedom (DOF) robotic manipulator arm, hereafter referred to as 'the arm' (ViperX300 s, Trossen Robotics) fitted with a 6-DOF force–torque load cell (FT300, Robotiq) at the end-effector (EE) base. A base plate apparatus, fitted with 1-DOF load-cell (H3-C3-25KG, Zemic), housed various counter-surfaces (CS) and was positioned adjacent to the arm (Fig. 1).

The arm and base plate were mounted on top of a floating optical table (Nexus, Thorlabs). A web camera (BRIO 4 K, Logitech) captured videos at 30 fps of the attachment–detachment cycles. The arm's joint motors power and load cells readings were sampled at a frequency of 100 Hz. The arm, load cells, and video camera were wired to a dedicated workstation that ran the experimental protocol program and logged the sensor data.

The gecko adhesive tape (DA910B, Setex) was cut from a larger sheet into 20 x 20 mm square patches and bonded with a double sided pressure sensitive adhesive (DSPSA) to a 5 mm thick ethylene propylene diene monomer (EPDM) foamed rubber spacer. The stack was then bonded to the distal end of the EE using additional DSPSA with the gecko tape facing outward. The foam spacer compensates for potential misalignment during operation, and introduces compliance between the EE and CS. A new piece of gecko adhesive tape was used in each experimental run, each consisting approximately 1,100 attachment–detachment cycles. A scanning electron micrograph (SEM) shows the microstructure of the gecko tape:

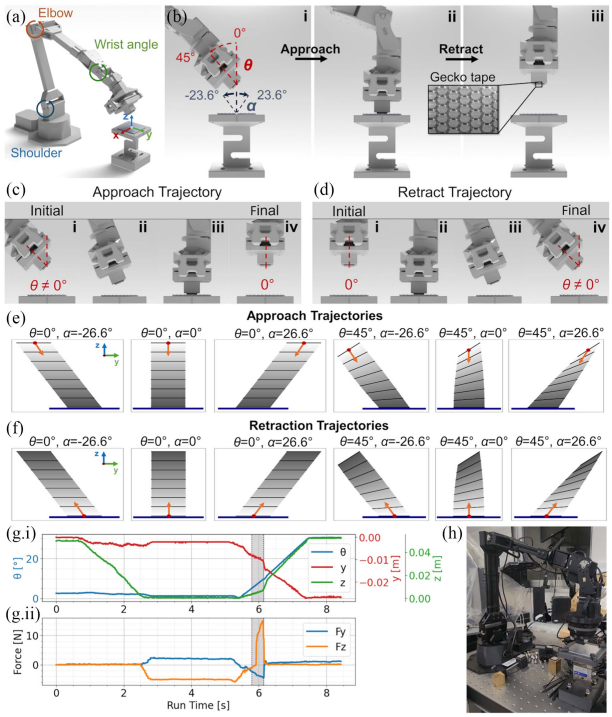

Fig. 1. (a) A computer aided design (CAD) visualization of the experimental setup shows the arm and base plate apparatus in the upright configuration. (b) The trajectory parameters θ & α angles for approach (i-ii) and retraction (ii-iii). (c) Approach trajectory sequence, governed by the initial θ & α. (d) Retraction trajectory sequence, governed by the final θ & α. (e)+(f) Visualizations of several approach and retraction trajectories. Each black line represents the adhesive pose in the $Y - Z$ plane during EE movement. The background transition from light to dark gray represents earlier to later frames in time, respectively. The CS is represented by a thick dark blue line at the lower part of each illustration. (e) Initial θ & α values and their associated approach trajectories. The EE is moving toward the base plate. (f) Final θ & α values and their associated retraction trajectories (the EE moves away from the base plate). (g) EE state variables (i) and normal and shear forces (ii) vs time. (h) A photo of the experimental setup.

perpendicular pillars (140 μm in height and 60 μm in diameter) with discoidal tips (140 μm in diameter). (Fig. 1(b),(ii)). All experiments were conducted under standard laboratory conditions: $50 \pm 10\,\%$ relative humidity, at $\mathrm{T} = 23 \pm 2\,°\mathrm{C}$

B. Upright and Inverted Experimental Configurations

The experiments were performed in both upright (normal) (Fig. 1) and inverted (Fig. 2) configurations. In the former, the base plate was mounted on top of the optical table with the CS facing upward, allowing the EE to approach it from above. Here, gravity assists attachment and opposes detachment (Fig. 1(a), video S1 & S2). In the latter, the base plate was mounted on a bridged assembly above the arm, with the CS facing downward so that the EE approaches it from below. In this case, gravity acts in the opposite direction—opposing attachment and assisting detachment (Fig. 2(a), Video S3 & S4).

The setup coordinate system was defined identically across both configurations to ensure that the relative motion between the EE and the CS remains consistent. It was set at the center of the outward CS face. A uniform preload pressure of 25 ± 2 kPa in the Z-axis ensured full engagement of the gecko-tape with the CS. The positive Y-axis was aligned with the arm's extension

IEEE Robotics and Automation Letters (RA-L) paper, presented at ICRA 2026, Vienna, Austria. Cite as RA-L paper.

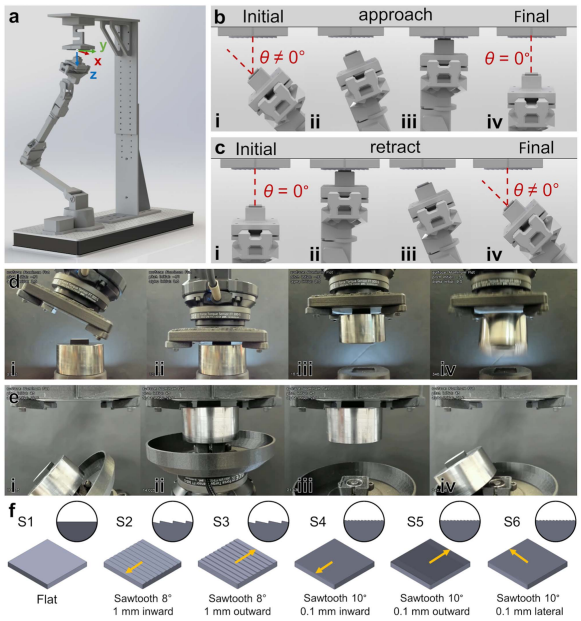

Fig. 2. (a) A CAD visualization of the experimental setup in the inverted configuration. Movement sequence of approach (b) and retraction (c) trajectories. Weight attachment sequence in the upright (d) and inverted (e) configurations. (f) CSs S1-S6, their geometries and orientations.

direction, while the positive Z-axis pointed along the outward normal of the CS. The X-axis was determined using the right-hand rule with respect to the Y- and Z-axes.

C. Approach & Retraction Trajectories

We define two types of trajectories: the approach trajectory, used for attachment, and the retraction trajectory, used for detachment. These trajectories are defined by two angular parameters: the pitch angle θ, and the trajectory angle α (Fig. 1(b),(i)).

The pitch angle θ describes the orientation of the EE around the *X*-axis at the onset and end of movements for approach and retraction, respectively. It varies between $0°$ and $45°$, where $\theta = 0°$ corresponds to the adhesive surface being parallel to the CS. The trajectory angle α specifies the EE direction of motion in the *Y–Z* plane and is defined as:

$$\alpha = \arctan\left(\frac{y_{start} - y_{goal}}{z_{start} - z_{goal}}\right) \tag{2}$$

It ranges between $\pm 23.6°$. with positive values of α corresponding to motion within the first quadrant of the *Y–Z* plane, and negative values corresponding to motion within the second quadrant. An angle of $\alpha = 0°$ denotes motion along the *Z*-axis.

We define the EE state vector $\mathbf{X}(t)$ as follows:

$$\mathbf{X}(t) = \begin{bmatrix} y(t) \\ z(t) \\ \theta(t) \end{bmatrix}, \; x_i(t) = x_{\text{start}} + \frac{t}{T}\left(x_{\text{goal}} - x_{\text{start}}\right), \; t \in [0, T] \tag{3}$$

where $x_i(t)$ is the instantaneous state at time t, parameterized between x_{start} and x_{goal}, and T is the trajectory overall execution time.

The approach trajectory motion sequence is illustrated in Figs. 1(c) and 2(b) for the upright and inverted configurations, respectively: (i) the EE is positioned at $\mathbf{x}_{start} = [\, y_i, z_i, \theta_i \,]^{\mathsf{T}}$; (ii) the EE follows the approach trajectory towards $\mathbf{x}_{goal} = [\, y_{ad}, z_{ad}, \theta_{ad} \,]^{\mathsf{T}}$; (iii) the adhesive attaches to the CS and the arm pauses; (iv) the EE follows a complementary retraction trajectory (vertical movement) from $\mathbf{x}_{start} = [\, y_{ad}, z_{ad}, \theta_{ad} \,]^{\mathsf{T}}$ towards $\mathbf{x}_{goal} = [\, 0, z_f, 0 \,]^{\mathsf{T}}$ and the adhesive detaches from the CS, (see Video S1 & S3 in the Supporting Information).

The retraction trajectory motion sequence is illustrated in Figs. 1(d) and 2(c) for the upright and inverted configurations respectively: (i) the EE is positioned at $\mathbf{x}_{start} = [\, 0, z_i, 0 \,]^{\mathsf{T}}$; (ii) the EE follows a complementary approach trajectory (vertical movement) towards $\mathbf{x}_{goal} = [\, y_{ad}, z_{ad}, \theta_{ad} \,]^{\mathsf{T}}$, the adhesive attaches to the CS and the arm pauses; (iii) the EE follows the retraction trajectory from $\mathbf{x}_{start} = [\, y_{ad}, z_{ad}, \theta_{ad} \,]^{\mathsf{T}}$ towards $\mathbf{x}_{goal} = [\, y_f, z_f, \theta_f \,]^{\mathsf{T}}$ and the adhesive detaches from the CS; (iv) the EE reaches $\mathbf{x}_{goal}$, (see Video S2 & S4).

The EE was confined to move only in the *Y–Z* plane and around the *X* axis during the approach and retraction trajectories. Therefore, only three of the six joint motors: shoulder, elbow and wrist angles, marked with blue, orange, and green circular arrows, respectively, participated in the movement (Fig. 1(a)). The adhesion position was set at the system origin: $[\, y_{ad}, z_{ad}, \theta_{ad} \,]^{\mathsf{T}} = [0]$.

A motion following a trajectory – determined by the combination of θ & α values, exerted varying stresses on the adhesive-surface interface during attachment and detachment, which in turn either enhanced or reduced adhesion strength. A motion along a trajectory representative graph (Fig. 1(g)) shows the instantaneous changes of the EE state variables $[\, y(t), z(t), \theta(t) \,]^{\mathsf{T}}$ (Fig. 1(g).(i)), together with the measured forces $[\, F_y, F_z \,]^{\mathsf{T}}$ acting on the EE-CS interface, throughout the attachment-detachment cycle (Fig. 1(g),(ii)). In that graph, as the EE pushes against the CS at $t \approx 2.5\,\text{s}$, F_y and F_z forces exert shear and compressive stresses, respectively, that preload the adhesive tape. Upon retraction, the combined movement along y, z, and θ exert stresses that oppose adhesion. These stresses reverse sign and increase until complete separation of the adhesive from the CS at $t \approx 6.1\,\text{s}$.

D. Counter-Surfaces Design and Morphology

Six different 70 x 70 mm aluminum 6061 alloy CSs (Fig. 2(f)) were used to examine how variations in surface geometry, orientation, and scaling influence trajectory optimization. The CSs are designated as follows: S1 – flat surface, S2 – sawtooth pattern with base acute angle of $8°$ and a height of 1 mm, the hypotenuse normal direction lies within the second quadrant of the $Y - Z$ plane ($Y < 0, Z > 0$). S3 – the same geometry as S2, but rotated in $180°$, S4 – sawtooth pattern with base acute angle of $10°$ and a height of 0.1 mm, the hypotenuse normal direction lies within the second quadrant of the Y-Z plane, S5 – the same geometry as S4, but rotated in $180°$, S6 – the same geometry as S4, but rotated in $90°$.

E. Picking and Attaching Objects

We examine the optimization of gecko-inspired adhesion in additional two real-life cases: (1) picking up an object and;

IEEE Robotics and Automation Letters (RA-L) paper, presented at ICRA 2026, Vienna, Austria. Cite as RA-L paper.

(2) attaching an object to inverted surfaces. To this end, a 760 g metal cylindrical weight (Fig. 2(d), (e)) was attached to the S1 CS using the arm. We defined the parameter t_a (adhesion duration), as the time interval between the moment the weight was fully suspended from the CS and the moment it completely detached and fell. For picking up an object, the weight was placed on a platform while the CS was mounted on the EE. The experiment is depicted in Fig. 2(d): (i) the EE approaches the weight; (ii) attaches, and; (iii) moves up in the Z direction with the weight. (iv) The weight detaches after t_a (video S5 & S6).

For attaching an object to an inverted surface, the EE lifts the weight and brings it to the upper surface. The gecko-tape in both cases is glued to the weight using DSPSA. The sequence is depicted in Fig. 2(e): (i) an electromagnet is used to hold the weight during movement of the EE, (ii) the weight is attached to the counter surface with the gecko adhesive and the electromagnet is deactivated; (iii) the EE retracts, leaving the weight attached to the CS, (iv) the weight detaches after t_a (videos S7 & S8).

F. Adhesion Strength Processing and Evaluation

In each attachment-detachment cycle, the adhesion strength was evaluated using two metrics during detachment for both the approach and the retraction trajectories: tensile strength and motor energy expenditure. The former was measured with the base plate load-cell, which recorded an increasing force during retraction until it reached a peak value prior to detachment. The latter was derived from the motor current readings, which was then integrated from the onset of tensile loading to the point of full separation, yielding the arm's energy expenditure during detachment.

We applied nonlinear regression using a power-law function to model the relationship between motor energy expenditure and maximal tensile stress, (see S1). The model reveals a strong positive correlation between the two metrics during detachment. However, only the energy expenditure was used for the optimization objective function.

To compare between unoptimized and optimized trajectories, each surface's adhesion strength was normalized to the maximum adhesion strength obtained under the unoptimized case per configuration, and objective:

$$A^{*} = \frac{Adhesion\ strength}{max(unoptimized\ Adhesion\ Strength)} \tag{4}$$

To compare between trajectories yielding maximum and minimum adhesion strength, each surface's adhesion strength was normalized by dividing it by the maximum adhesion strength per configuration and objective.

$$A^{**} = \frac{Adhesion\ strength}{max(Adhesion\ Strength)} \tag{5}$$

G. Attachment - Detachment Cycles

For each CS, approach and retraction trajectories were examined under both minimization and maximization objectives, yielding four optimization cases: (1) approach minimum, (2) approach maximum, (3) retraction minimum, and (4) retraction maximum (Fig. 3(a)). Each objective was repeated five times (five runs). Each run included 110 evaluations until convergence to a global optimum. Thus, each objective required 550 evaluations, and 1,100 were used to construct the full trajectory solution space.

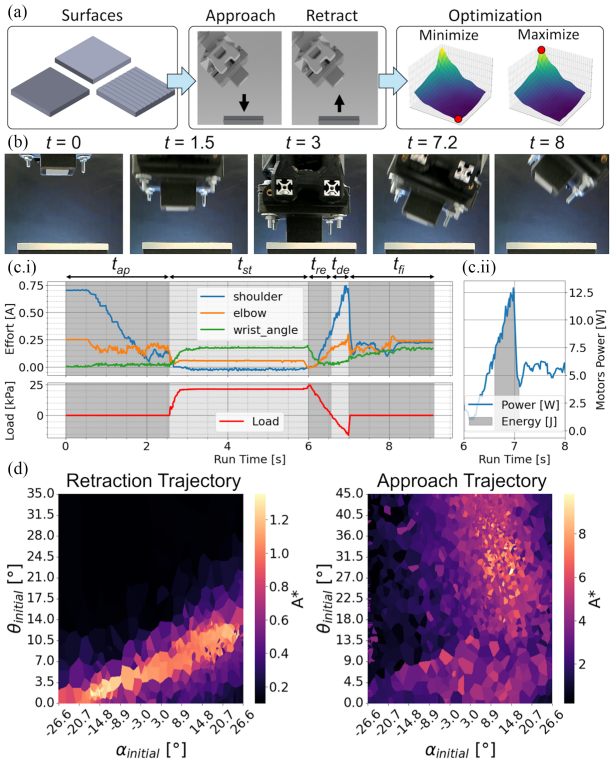

Fig. 3. (a) Experimental flow-chart of the trajectory optimization of an arm with gecko-inspired adhesive. Each optimization was specific to one of six CSs, one of two trajectories: approach or retraction, one of two objectives: minimization or maximization and one of two configurations: upright or inverted. We call this combination "CS-trajectory objective". In total, 24 unique CS-trajectory objective optimizations were performed in each configuration. (b) Time series of the EE during attachment-detachment cycle. (c) i. Time series of joint motor currents and load-cell readings. ii. The power and energy consumption of the motors at t_{de}. (d) A representative heat map of the normalized adhesion strength ($A*$) as a function of θ & α angles in approach and retraction trajectories. A smooth transition between low and high adhesion strength regions is visible.

Fig. 3(b) shows a representative attachment-detachment cycle, in which the arm approaches ($t = 0$-1.5 s), attaches ($t = 3$ s), detaches ($t = 7.2$ s) and retracts ($t \geq 8$ s) from the CS. Motor currents (Effort) of the arm's joints are shown in blue, orange, and green, alongside base plate tensile readings (Load) in red (Fig. 3(c)). Each attachment-detachment cycle consists of five stages. In t_{ap} the arm moves from its initial pose until it makes contact with the CS. In t_{st} the arm pushes against the CS until the predefined preload is reached, the arm then stops and remains static. In t_{re} the arm moves away from the CS, and the preload stress decreases until it reaches zero. In t_{de} the EE moves away while still attached to the CS, generating an increasing tensile stress until the maximum adhesion strength is reached and detachment occurs. Lastly, in t_{fi} the EE completes its movement towards the final position.

In order to identify the exact time intervals of the different stages, we used the base plate load-cell to measure the adhesion

IEEE Robotics and Automation Letters (RA-L) paper, presented at ICRA 2026, Vienna, Austria. Cite as RA-L paper.

tensile stresses in-situ. A representative tensile stress plot is shown in red, below the effort measurements. Positive values correspond to compressive (preload) stresses, while negative values indicate tensile adhesion stresses. An adhesion strength heat map, composed of the full trajectory solution space is shown in (Fig. 3(d)) where lighter colors represent higher adhesion strength.

H. Trajectory Optimization Scheme

We employed particle swarm optimization (PSO) to optimize the approach and retraction trajectory parameters θ & α according to the following objective function. Let the vector of decision variables be $\mathbf{x} = \langle x_1, x_2 \rangle$.

The goal is to minimize or maximize:

$$f_{\text{obj}}(\mathbf{x}) = \sum_{i=1}^{n} \left(\int_{t_{\text{zero preload}}}^{t_{\text{detachment}}} I_{\text{motor } i}(t) \cdot V_{\text{motor } i} \, dt \right), \qquad n = 3 \tag{6}$$

where:

x_1 = the initial/final θ angle, x_2 = the initial/final α angle.

f_{obj} = arm's motor energy consumption during detachment. PSO was selected for its computational efficiency, simplicity, and robustness in exploring large search spaces, while avoiding local optima. The algorithm iteratively updates a swarm of candidate solutions ("particles") based on individual and collective best positions. As PSO does not rely on gradient information, it is well suited for non-differentiable and noisy objective functions, such as in our setup, where the objective is evaluated through physical measurements.

In each optimization iteration, the EE executed an attachment–detachment cycle, after which the objective function evaluated the resulting adhesion strength. A new trajectory was then generated based on the convergence direction across the θ & α angles. The process continued until reaching the maximum number of evaluations, with a swarm size of 10 particles and 10 iterations per particle (110 evaluations in total). The minimum step size and objective function change threshold were both set to 0.05.

I. Statistical Analysis

Statistical analyses were conducted to evaluate whether the optimized trajectories significantly improved adhesion performance relative to the baseline condition. Differences between the optimized and baseline means were assessed using Welch's two-sample t-test, which accounts for unequal variances and sample sizes. For each comparison, the mean difference and its 95% confidence interval (CI) were computed from the t-distribution using the Welch–Satterthwaite approximation for degrees of freedom. Optimization results were considered valid when the improvement over the baseline was statistically significant ($p < 0.05$) and the 95% CIs of the two trajectories did not overlap.

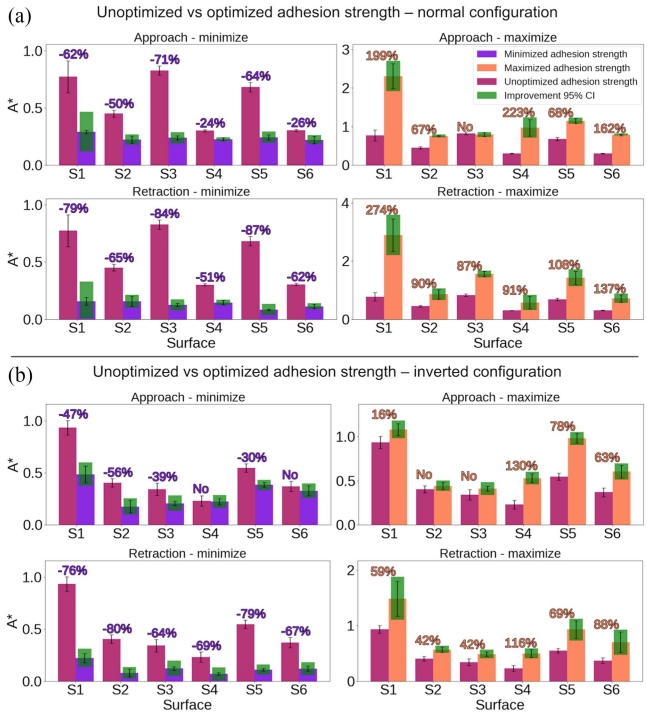

Fig. 4. The normalized adhesion strength (A^*) as a function of CS-trajectory objective, in each of the six CSs (S1–S6). The results are separated to four subplots, one for each trajectory objective in the upright (a) and inverted (b) configurations. The percent improvement between the unoptimized and optimized adhesion strength is shown in colored texts above the bars.

J. Data Availability

The data and code supporting this study are openly available on the Open Science Framework (OSF) at https://osf.io/743cb.

III. Results

A. Optimized Trajectories for Enhanced Adhesion

The trajectory optimization results of the upright and inverted configurations are shown in Fig. 4(a), (b), respectively. Each configuration is divided to four trajectory objective subplots: approach minimize, approach maximize, retraction minimize, and retraction maximize. Six CSs (Fig. 4(c)) were tested in each trajectory objective, resulting in a total of 48 experimental scenarios. We compare the normalized adhesion strengths obtained for each CS (S1–S6) across different trajectory objectives, and indicate the percentage change relative to the unoptimized adhesion strength above each bar. We use the normalized adhesion strength A^*.

The pink bars show the unoptimized adhesion strengths, obtained when the arm follows a trajectory constrained to the Z axis (θ & α equal to zero). This serves as a reference to the optimized adhesion strength. Purple and orange bars show the minimized and maximized adhesion strengths, respectively, for each scenario. The percent change relative to the unoptimized reference is noted above each bar in color-coded text. A green bar overlay represents 95% CI improvement relative to the unoptimized adhesion strength. CSs S1–S6 are shown on the horizontal axis.

IEEE Robotics and Automation Letters (RA-L) paper, presented at ICRA 2026, Vienna, Austria. Cite as RA-L paper.

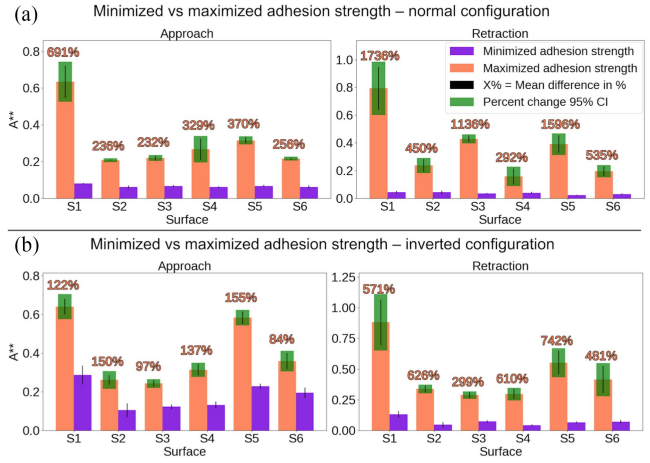

Fig. 5. A comparison of the normalized adhesion strength (A^{**}) results between the minimization and maximization objectives for each trajectory. The percent change between the optima results of CSs S1–S6 are shown for the upright (a) and inverted (b) configurations, and noted above the bars in orange colored text.

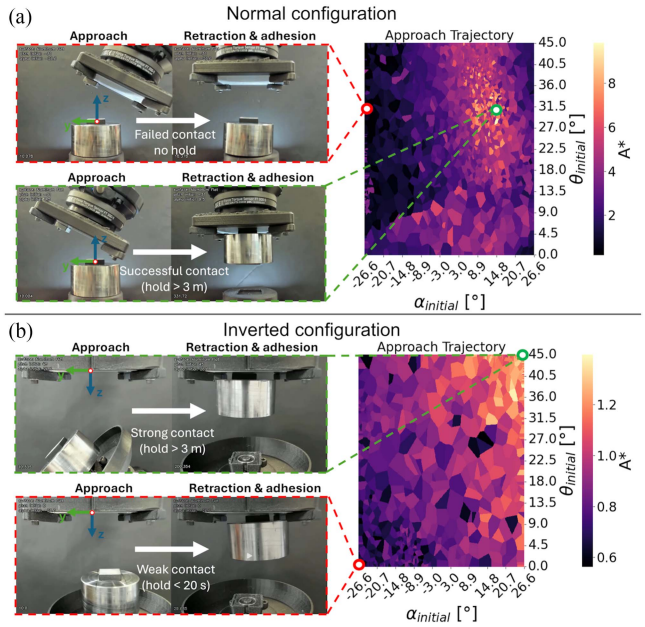

Fig. 6. Object attachment experiment summary of upright (a) and inverted (b) configurations. The approach trajectory optimization results are shown on the right side by a heat map, the adhesion duration of the metal weight is written in white text on the left side. In the heat map, a darker and lighter colors correspond to lower and higher adhesion strengths, respectively. The adhesion strength, which depends on the initial trajectory, correlates with the adhesion duration, t_a, of the metal weight.

The adhesion performance of the gecko tape was significantly improved in 43 out of 48 scenarios (89.5% success rate), with increases ranging from 16% to 274% under maximize optimizations and reductions from −24% to −87% under minimize optimizations. In the remaining five scenarios, the results fell within the error margins. The maximum adhesion strength of the approach (applying the adhesive) increased by 67% to 223% and 16% to 130% in the upright and inverted configurations, respectively. The minimum adhesion strength of the retraction (removing the adhesive) reduced by −24% to −71% and −64% to −80% in the upright and inverted configurations, respectively. The optimization results, including 95% CIs and p-values, are presented in Tables T1 and T2 (see *J. Data Availability*). Overall, the optimal adhesion strength varied depending on the CS geometry and orientation. Adhesion to the flat CS (S1) consistently produced higher absolute adhesion strength values compared to the sawtooth CSs, which had a reduced contact area due to their textured geometry.

B. Minimized Versus Maximized Adhesion Strengths

We now present the results combining the minimized and maximized objectives into an aggregated single subplot, excluding the unoptimized trajectory results. Fig. 5 shows the difference between the minimum and maximum adhesion strengths in terms of percent change. Here we use the normalized adhesion strength A^{**}.

The purple and orange bars denote the same quantities as before. Both optima are plotted for each CS (indexed S1–S6) across all trajectory objectives. The percent change between the minimum and maximum adhesion strengths for each CS is indicated in orange text above the bars.

A significant change between the minimized and maximized adhesion strengths is evident for each trajectory and CS. This demonstrates that both improved adhesion and easier detachment can be achieved by selecting the appropriate optimal trajectory. The comparison reveals percent changes ranging from 232% to 1736% in the upright configuration and 97% to 742% in the inverted configuration. The optimization results, including 95% CIs and p-values, are presented in Tables T3 and T4 (see *J. Data Availability*).

C. Improving Object Attachment to Surfaces With Trajectory Optimization

Based on the results from the optimization section, we evaluated the ability of our system to enhance the attachment of objects to a flat CS (S1). Furthermore, we examined whether the approach trajectory and the resulting adhesion strength correlate with the adhesion duration (t_a) of the attached object.

The experiments confirm that the optimal trajectories, identified through the optimization process, yield adhesion durations proportional to their corresponding adhesion strengths (Fig. 6(a),(b)). The trajectories with θ and α angles yielding the highest adhesion strength ($[31°, 9.5°]$ and $[45°, 26.6°]$) produced adhesion durations exceeding 3min, whereas those with the lowest ($[31°, -26.6°]$ and $[0°, -26.6°]$) resulted in no hold or detachment within 20 s.

IV. Discussion

This study demonstrates that adhesion performance of gecko-inspired adhesives can be significantly enhanced through trajectory optimization, revealing that there exists an energetically favorable path for a manipulator arm to approach and retract from a surface. Embedding such reversible adhesion mechanisms into robotic arms establishes a critical link between the physical principles of adhesion and the robot's dynamic

IEEE Robotics and Automation Letters (RA-L) paper, presented at ICRA 2026, Vienna, Austria. Cite as RA-L paper.

trajectory, showing that adhesion efficiency cannot be decoupled from the kinematic uncertainties, such as positional and orientational errors due to factors such as finite rigidity, structural compliance, and motor control limitations, inherent to robotic operation. These discrepancies create a mismatch between the calculated trajectory and the actual motion, resulting in lowered adhesion performance and detachment efficiency. Furthermore, conventional adhesion-strength measurements typically assume a rigid test apparatus and often neglect the compliance of the mechanical system. In robotic setups, the arm and EE deform during attachment and detachment, thus the actual preload and stresses during detachment differ from the commanded trajectory. As a result, adhesion strength depends not only on the adhesive–CS interaction, but also by the structural and spatial stiffness of the robotic arm. These insights are broadly relevant to the design of adaptive, energy-efficient robotic systems and is exemplified here through the presented model.

We leverage the PSO algorithm in order to improve adhesion and facilitate detachment between an arm and a CS, and demonstrate that the adhesion strength of gecko-inspired adhesives is highly sensitive to the approach and retraction trajectories. Specifically, for the same adhesive-CS combination, adhesion is governed by the preload stresses during approach and the pull-off stresses during retraction, and is primarily influenced by two key parameters: (1) the general movement vector toward or away from the CS (α angle), and (2) the EE tilting angle relative to the normal of the CS (θ angle). Our findings reveal up to 274% increase in adhesion strength when comparing between optimized versus unoptimized trajectories. Moreover, we observed a difference of up to 1736% between the minimum and maximum adhesion strengths within the same trajectory, highlighting the critical role of precise motion control in adhesion performance.

These findings have two key implications. First, increased adhesion strength at footholds can enhance the stability of robotic climbers and grippers, improving their ability to withstand unexpected forces and moments, and enable the robot to carry heavier payloads. Second, during climbing or gripping, a robot must repeatedly and efficiently detach and reattach its feet as it transitions between footholds. It is important to note that these applications require expanding the range of trajectories, particularly for systems with passive or flexible joints. Specifically, grasping stabilizes external objects through multiple contact points under variable loads, whereas climbing supports body movement via gait-synchronized attachment cycles under gravity-dominated normal and shear forces. In any case, the ability to reversibly detach from surfaces with minimal energy expenditure is crucial for efficient energy management, enabling longer operational missions and access to larger climbing surfaces. Additionally, low-energy detachment improves overall stability by minimizing abrupt motions.

A key limitation of the proposed optimization framework, as with other optimization methods, is its dependence on configuration, i.e. the results are specific to the setup, adhesive, CS properties, and arm used. Nonetheless, the methodology is broadly applicable to other robotic platforms, though validation under real-world conditions (e.g uneven and contaminated surfaces) remains essential for practical implementation. In terms of the Kendall's peeling model, it relies on movement using one degree of freedom θ_k. In our system, we optimize the energy based on two degrees of freedom and therefore, obtain different dependencies on the positioning and movement of the end-effector. Furthermore, the use of a rigid end-effector renders the case of $\theta_k = 0$ redundant, since the gecko-tape cannot fold. We also point out a fundamental difference between dry adhesives integrated in robotic systems and the Kendall theoretical model. The latter assumes detachment through crack propagation, determined from a force per unit width of the adhesive, while in our case the adhesion strength is used for the optimization, and is additionally coupled to the stiffness of the robotic arm.

Synthetic dry adhesives for climbing robots and grippers still face challenges of limited surface conformability and contamination-induced adhesion loss, that optimization can mitigate. Addressing these challenges is essential for ensuring the long-term reliability and effectiveness of dry adhesives in real-world environments, and will compliment the mechanism reported in this study. In the future, AI-driven optimization will enable real-time autonomous control of preload and detachment, potentially improving performance and mitigating gecko-tape deterioration over repeated adhesion cycles.

APPENDIX A
FIGURES

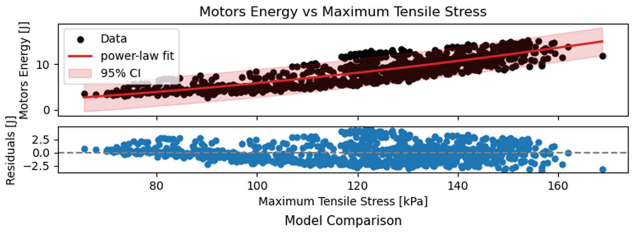

Model Comparison

Model	Equation	AIC	BIC	CV RMSE
Power law	$E = a\sigma^b$	946.29	956.22	1.564
Quadratic	$E = a\sigma^2 + b\sigma + c$	947.76	962.65	1.565
Linear	$E = a\sigma + b$	971.86	981.79	1.582

Fig. 7. motor energy vs adhesion strength nonlinear regression model using a power-law function: $E = a\,\sigma^b$ where E is motor energy (J) and σ is maximum tensile stress (kPa). This model obtained the best fit between the linear and quadratic models. The fitted parameters were $a = 1.49 \times 10^{-3}$ $[0.93,\ 2.05] \times 10^{-3}$ and $b = 1.80\,[1.72,\ 1.87]$ (95 % confidence intervals). The model achieved AIC = 946.3, BIC = 956.2, and a cross-validated RMSE = 1.56 J. The exponent $b > 1$ demonstrates that adhesion energy grows faster with applied stress, indicating progressively higher mechanical work at increased load. Residuals showed no systematic bias and approximately constant variance, confirming the adequacy of the model.

ACKNOWLEDGMENT

We thank Dr. Avishai Sintov from the School of Mechanical Engineering, Tel Aviv University, Israel, for fruitful discussions and insightful advices.

REFERENCES

[1] E. Kroner, E. Arzt, and G. Adhesion, *Encyclopedia of Nanotechnology*, B. Bhushan, Ed. Dordrecht, Netherlands: Springer, 2016.
[2] T. Materzok, H. Eslami, S. N. Gorb, and F. Müller-Plathe, "Understanding humidity-enhanced adhesion of geckos: Deep neural network-assisted

multi-scale molecular modeling," *Small*, vol. 19, p. 2206085, 2023, doi: 10.1002/smll.202206085.
[3] C. T. Mitchell, C. B. Dayan, D.-M Drotlef, M. Sitti, and A. Y. Stark, "The effect of substrate wettability and modulus on gecko and gecko-inspired synthetic adhesion in variable temperature and humidity," *Sci. Rep.*, vol. 10, no. 1, 2020, Art. no. 19748.
[4] B. Soltannia and D. S. Sameoto, "Reversible underwater adhesion via gecko-inspired hydrophobic fibers," *ACS Appl. Mater. Interfaces*, vol. 6, no. 24, pp. 21995–22003, 2014.
[5] Y. Wang, R. Hensel, and E. Arzt, "Attachment of bioinspired microfibrils in fluids: Transition from a hydrodynamic to hydrostatic mechanism," *J. Roy. Soc. Interface*, vol. 19, no. 189, 2022, Art. no. 20220050.
[6] S. H. Lee, H. W. Song, H. J. Park, and M. K. Kwak, "Surface adaptable and adhesion controllable dry adhesive with shape memory polymer," *Macromol. Rapid Commun.*, vol. 43, no. 8, 2022, Art. no. 2200012.
[7] W. Wang, Y. Liu, and Z. Xie, "Gecko-like dry adhesive surfaces and their applications: A review," *J. Bionic Eng.*, vol. 18, no. 5, pp. 1011–1044, 2021.
[8] S. A. Suresh, A. Hajj-Ahmad, E. W. Hawkes, and M. R. Cutkosky, "Forcing the issue: Testing gecko-inspired adhesives," *J. Roy. Soc. Interface*, vol. 18, no. 174, 2021, Art. no. 20200730.
[9] M. Kamperman, E. Kroner, A. del Campo, R. M. McMeeking, and E. Arzt, "Functional adhesive surfaces with 'gecko' effect: The concept of contact splitting," *Adv. Eng. Mater.*, vol. 12, no. 5, pp. 335–348, 2010.
[10] D. Tan et al., "Switchable adhesion of micropillar adhesive on rough surfaces," *Small*, vol. 15, no. 50, 2019, Art. no. 1904248.
[11] Y. Mengüç, M. Röhrig, U. Abusomwan, H. Hölscher, and M. Sitti, "Staying sticky: Contact self-cleaning of gecko-inspired adhesives," *J. Roy. Soc. Interface*, vol. 11, no. 94, 2014, Art. no. 20131205.
[12] Z. Wang, P. Gu, and X. Wu, "A gecko-inspired double-sided adhesive," *Phys. Chem. Chem. Phys.*, vol. 15, no. 47, pp. 20764–20770, 2013.
[13] J.-S Kwak and T.-W Kim, "A review of adhesion and friction models for gecko feet," *Int. J. Precis. Eng. Manuf.*, vol. 11, no. 1, pp. 171–186, 2010.
[14] J. Yu et al., "Gecko-inspired dry adhesive for robotic applications," *Adv. Funct. Mater.*, vol. 21, pp. 3010–3018, 2011.
[15] J. Berengueres, S. Saito, and K. Tadakuma, "Structural properties of a scaled gecko foot-hair," *Bioinspiration Biomimetics*, vol. 2, no. 1, Jan. 2007, Art. no. 1.
[16] K. Takahashi, J. Berengueres, K. J. Obata, and S. Saito, "Geckos' foot hair structure and their ability to hang from rough surfaces and move quickly," *Int. J. Adhesion Adhesives*, vol, 26, no. 8, pp. 639–643, 2006.
[17] W. Ruotolo, D. Brouwer, and M. R. Cutkosky, "From grasping to manipulation with Gecko-inspired adhesives on a multifinger gripper," *Sci. Robot.*, vol. 6, no. 61, 2021, Art. no. eabi9773.
[18] T. T. Hoang, J. J. S. Quek, M. T. Thai, P. T. Phan, N. H. Lovell, and T. N. Do, "Soft robotic fabric gripper with Gecko adhesion and variable stiffness," *Sensors Actuators Phys.*, vol. 323, 2021, Art. no. 112673.
[19] S. Song, D.-M. Drotlef, C. Majidi, and M. Sitti, "Controllable load sharing for soft adhesive interfaces on three-dimensional surfaces," *Proc. Nat. Acad. Sci.*, vol. 114, no. 22, pp. E4344–E4353, 2017.
[20] E. Shahabi, F. Visentin, A. Mondini, and B. Mazzolai, "Octopus-inspired suction cups with embedded strain sensors for object recognition," *Adv. Intell. Syst.*, vol. 5, no. 2, 2023, Art. no. 2200201.
[21] D. Sameoto, H. Khungura, F. H. Benvidi, A. Asad, T. Liang, and M. Bacca, "Chapter fifteen - space applications for gecko-inspired adhesives," in *Biomimicry for Aerospace*, V. Shyam, M. Eggermont, and A. F. Hepp, Eds. New York, NY, USA: Elsevier, 2022, pp. 423–458.
[22] Z. Yu et al., "A Gecko-inspired robot using novel variable-stiffness adhesive paw can climb on rough/smooth surfaces in microgravity," *Adv. Intell. Syst.*, vol. 6, 2024, Art. no. 2400043.
[23] D. Feldmann, R. Das, and B.-E Pinchasik, "How can interfacial phenomena in nature inspire smaller robots," *Adv. Mater. Interfaces*, vol. 8, no. 1, 2021, Art. no. 2001300.
[24] D. Santos, M. Spenko, A. Parness, S. Kim, and M. Cutkosky, "Directional adhesion for climbing: Theoretical and practical considerations," *J. Adhesion Sci. Technol.*, vol. 21, no. 12/13, pp. 1317–1341, 2007.
[25] J. P. Dıáz Téllez, D. Sameoto, and C. Menon, "Cleaning properties of dry adhesives," *Sci. China Technol. Sci.*, vol. 53, no. 11, pp. 2942–2946, 2010.
[26] J. Berengueres, M. Urago, S. Saito, K. Tadakuma, and H. Meguro, "Gecko inspired electrostatic chuck," in *Proc. IEEE Int. Conf. Robot. Biomimetics*, Kunming, China, 2006, pp. 1018–1023.
[27] B. Zhang, Y. Xie, J. Zhou, K. Wang, and Z. Zhang, "State-of-the-art robotic grippers, grasping and control strategies, as well as their applications in agricultural robots: A review," *Comput. Electron. Agriculture*, vol. 177, 2020, Art. no. 105694.
[28] J. Qu, Z. Yu, W. Tang, Y. Xu, B. Mao, and K. Zhou, "Advanced technologies and applications of robotic soft grippers," *Adv. Mater. Technol.*, vol. 9, no. 11, 2024, Art. no. 2301004.
[29] D. Cruz-Ortiz, M. Ballesteros-Escamilla, I. Chairez, and A. Luviano, "Output second-order sliding-mode control for a Gecko biomimetic climbing robot," *J. Bionic Eng.*, vol. 16, no. 4, pp. 633–646, 2019.
[30] O. Unver, M. Murphy, and M. Sitti, "Geckobot and waalbot: Small-scale wall climbing robots," in *Infotech@Aerospace*, American Institute of Aeronautics and Astronautics, 2005.
[31] Y. Song, X. Lu, J. Zhou, Z. Wang, Z. Zhang, and Z. Dai, "Geckos distributing adhesion to toes in upside-down running offers bioinspiration to robots," *J. Bionic Eng.*, vol. 17, no. 3, pp. 570–579, 2020.
[32] D. Santos, B. Heyneman, S. Kim, N. Esparza, and M. R. Cutkosky, "Gecko-inspired climbing behaviors on vertical and overhanging surfaces," in *Proc. IEEE Int. Conf. Robot. Automat.*, 2008, pp. 1125–1131.
[33] L. Schiller, A. Seibel, and J. Schlattmann, "Toward a gecko-inspired," *Climbing Soft Robot. Front. Neurorobot.* 2019, pp. 13.
[34] O. Unver, A. Uneri, A. Aydemir, and M. Sitti, "Geckobot: A Gecko inspired climbing robot using elastomer adhesives," in *Proc. IEEE Int. Conf. Robot. Automat.*, 2006, pp. 2329–2335.
[35] J. Liu, Z. Tong, J. Fu, D. Wang, Q. Su, and J. Zou, "A gecko inspired fluid driven climbing robot," in *Proc. IEEE Int. Conf. Robot. Automat.*, 2011, pp. 783–788.
[36] C. Menon and M. Sitti, "A biomimetic climbing robot based on the Gecko," *J. Bionic Eng.*, vol. 3, no. 3, pp. 115–125, 2006.
[37] Z. Li, Q. Xu, and L. M. Tam, "A survey on techniques and applications of window-cleaning robots," *IEEE Access*, vol. 9, pp. 111518–111532, 2021.
[38] P. Sekhar and R. S. Bhooshan, "Duct fan based wall climbing robot for concrete surface crack inspection," in *Proc. Annu. IEEE India Conf.*, 2014, pp. 1–6.
[39] Q. Liu et al., "A novel nuclear station inspection robot," in *Proc. 4th IEEE Int. Conf. Inf. Sci. Technol.*, 2014, pp. 678–681.
[40] M. Sadeghi, A. Abbasimoshaei, J. P. Kitajima Borges, and T. A. Kern, "Numerical and experimental study of a wearable exo-glove for telerehabilitation application using shape memory alloy actuators," *Actuators*, vol. 13, 2024, Art. no. 409.
[41] A. Abbasimoshaei et al., "Design and impedance control of a hydraulic robot for paralyzed people," in *Proc. 8th RSI Int. Conf. Robot. Mechatron.*, 2020.
[42] D. Shao, J. Chen, A. Ji, Z. Dai, and P. Manoonpong, "Hybrid soft-rigid foot with dry adhesive material designed for a gecko-inspired climbing robot," in *Proc. 3rd IEEE Int. Conf. Soft Robot. RoboSoft*, 2020, pp. 578–585.
[43] Z. Yu, Z. Wang, R. Liu, P. Wang, and Z. Dai, "Stable gait planning for a Gecko-inspired robot to climb on vertical surface," in *Proc. IEEE Int. Conf. Mechatron. Autom.*, 2013, pp. 307–311.
[44] Z. Wang, G. Sun, and Z. Dai, "Trajectory optimization for robot crawling on ceiling using dry elastomer adhesive," in *Proc. Adv. Reconfigurable Mechanisms Robots II*, X. Ding, X. Kong, and J. S. Dai, Eds., Cham, Switzerland, Springer, 2016, pp. 593–601.
[45] S. Shi, S. Fang, X. Wu, and X. Wang, "Gait design and foot trajectory planning for a wall-climbing robot with spiny toes," in *Proc. Intell. Robot. Appl.*, X.-J. Liu, Z. Nie, J. Yu, F. Xie, and R. Song, Eds., Cham, Switzerland, Springer, 2021, pp. 825–835.
[46] K. Kendall, "Thin-film peeling-the elastic term," *J. Phys. D, Appl. Phys.*, vol. 8, no. 13, Sep. 1975, Art. no. 1449.
[47] K. Autumn, A. Dittmore, D. Santos, M. Spenko, and M. Cutkosky, "Frictional adhesion: A new angle on Gecko attachment," *J. Exp. Biol.*, vol. 209, no. 18, pp. 3569–3579, Sep. 2006.
[48] A. Jagota and S. J. Bennison, "Mechanics of adhesion through a fibrillar microstructure," *Integrative Comp. Biol.*, vol. 42, no. 6, pp. 1140–1145, 2002.
[49] S. Kim, M. Spenko, S. Trujillo, B. Heyneman, D. Santos, and M. R. Cutkosky, "Smooth vertical surface climbing with directional adhesion," *IEEE Trans. Robot.*, vol. 24, no. 1, pp. 65–74, Feb. 2008.